

VIP Very Important Paper

www.batteries-supercaps.org

Special Collection



# Microstructure Control of LiCoO<sub>2</sub>-Li<sub>10</sub>GeP<sub>2</sub>S<sub>12</sub> Composite Cathodes by Adjusting the Particle Size Distribution for the Enhancement of All-Solid-State Batteries

Yuto Yamada,<sup>[a]</sup> Kenta Watanabe,<sup>[a]</sup> Han-Seul Kim,<sup>[a]</sup> Kota Suzuki,<sup>[b]</sup> Satoshi Hori,<sup>[b]</sup> Ryoji Kanno,<sup>[b]</sup> and Masaaki Hirayama\*<sup>[a, b]</sup>

Microstructure control of composite electrodes comprising active materials and solid electrolytes is imperative to achieve sufficient ion- and electron-conductive pathways for the development of all-solid-state Li ion batteries. Here, we synthesized Li<sub>10</sub>GeP<sub>2</sub>S<sub>12</sub> solid electrolytes with various particle size distributions by milling and filtering. Impedance spectroscopy revealed that the ionic conductivities in the bulk were hardly changed by the synthetic processes. This enabled us to investigate only the microstructure effects on the electrochemical properties of the composite electrodes. Microscopic and electrochemical tests of the LiCoO<sub>2</sub>-Li<sub>10</sub>GeP<sub>2</sub>S<sub>12</sub> composite

cathodes clarified that the size distributions of the Li<sub>10</sub>GeP<sub>2</sub>S<sub>12</sub> drastically affected the microstructures in the composite cathodes, such as contacts at interfaces and voids between particles. The size distributions also contributed to the appropriate ratio of LiCoO<sub>2</sub> to Li<sub>10</sub>GeP<sub>2</sub>S<sub>12</sub> for superior charge/discharge properties. The (de)intercalation reversibly proceeded in the composite cathode using the filtered Li<sub>10</sub>GeP<sub>2</sub>S<sub>12</sub> even though the ratio of Li<sub>10</sub>GeP<sub>2</sub>S<sub>12</sub> decreased from 50% to 30% in volume. This study demonstrated the possibility of high-energy-density composite cathodes for all-solid-state batteries by control of microstructures in composite electrodes.

## Introduction

All-solid-state lithium-ion batteries (ASSBs) with sulfide solid electrolytes have attracted research attention as power sources in large-scale applications, due to their inherently high volumetric energy densities, high power characteristics, and high reliability.<sup>[1–3]</sup> However, their volumetric energy densities and power characteristics have been limited in most bulk type ASSBs using composite electrodes comprising active materials and solid electrolytes. One reason is the difficulty in designing the microstructure in the composite electrodes with high electronic and ionic conductivities and sufficient (de)intercalation sites between the active materials

and the solid electrolyte particles. To achieve a high volumetric energy density, the volumetric ratio of the active material to the solid electrolyte should be as high as possible. However, the reversible capacity and power characteristics of ASSBs are drastically degraded by the decrease in the ratio of the solid electrolyte compared with conventional lithium-ion batteries using liquid electrolytes. This is because the conduction pathways and (de)intercalation sites for Li ions between the particles drastically decrease due to the rigidity of the solid electrolyte.<sup>[2,4]</sup> Thus, in most electrode composites, which exhibit superior electrochemical properties, the volumetric ratios of the solid electrolyte to the active material are approximately 50%.<sup>[5–8]</sup> The volumetric energy density has been improved by the development of solid electrolytes with excellent ionic conductivities over 10<sup>–2</sup> S cm<sup>–1</sup> and/or electrode materials possessing good (de)intercalation abilities.<sup>[5,7,8]</sup> Furthermore, control of microstructures has been studied in composite electrodes to ensure sufficient conduction pathways and (de)intercalation sites even at the volumetric ratio of the solid electrolyte to the active material lower than 50%.<sup>[2,9]</sup>

Many theories have been proposed for the correlation between microstructure and the electrical conductivities of composite materials.<sup>[10–15]</sup> Electronic and ionic conductivities of a composite electrode are significantly affected by the particle size distribution of a solid electrolyte and an active material and their volumetric ratio. Regarding composite cathodes in sulfide-type ASSBs, charge/discharge capacities can be improved by changing the particle sizes of layered rock salt type Li<sub>1+x</sub>(Ni<sub>1-y-z</sub>Co<sub>y</sub>Mn<sub>z</sub>)<sub>1-x</sub>O<sub>2</sub> cathodes,<sup>[16]</sup> Li<sub>2</sub>S-P<sub>2</sub>S<sub>5</sub> glass electrolytes,<sup>[17]</sup> and by optimizing the ratio of LiNi<sub>1/3</sub>Mn<sub>1/3</sub>Co<sub>1/3</sub>O<sub>2</sub> cathode to Li<sub>3</sub>PS<sub>4</sub> glass electrolyte.<sup>[18]</sup> Most reports

[a] Dr. Y. Yamada, Prof. K. Watanabe, H.-S. Kim, Prof. M. Hirayama

Department of Chemical Science and Engineering  
School of Materials and Chemical Technology  
Tokyo Institute of Technology  
Yokohama 226-8502 (Japan)  
E-mail: hirayama@mac.titech.ac.jp

[b] Prof. K. Suzuki, Prof. S. Hori, Prof. R. Kanno, Prof. M. Hirayama

Research Center for All-Solid-State Battery  
Institute of Innovative Research  
Tokyo Institute of Technology  
Yokohama 226-8502 (Japan)

Supporting information for this article is available on the WWW under <https://doi.org/10.1002/batt.202300261>

This publication is part of a joint Special Collection on Solid State Batteries, featuring contributions published in Advanced Energy Materials, Energy Technology, Batteries & Supercaps, ChemSusChem, and Advanced Energy and Sustainability Research.

© 2023 The Authors. *Batteries & Supercaps* published by Wiley-VCH GmbH. This is an open access article under the terms of the Creative Commons Attribution License, which permits use, distribution and reproduction in any medium, provided the original work is properly cited.

have focused on composite cathodes using glass electrolytes with low ionic conductivities.  $\text{Li}_{10}\text{GeP}_2\text{S}_{12}$ -type and argyrodite-type crystalline electrolytes exhibit higher ionic conductivities and rigidities than glass electrolytes.<sup>[4,19]</sup> Therefore, crystalline electrolytes are expected to show different relationships between microstructures and electrochemical properties when applied to composite electrodes. Various composite electrodes have been constructed by using  $\text{Li}_{10}\text{GeP}_2\text{S}_{12}$ -type crystalline electrolytes.<sup>[5,20–24]</sup> However, there have been few studies on composite cathodes comprising oxide cathodes and crystalline sulfide electrolytes, such as  $\text{LiCoO}_2$ - $\text{Li}_{10}\text{GeP}_2\text{S}_{12}$  composites, which focus on charge/discharge properties depending on their mixing conditions<sup>[25]</sup> and their volumetric ratio.<sup>[6]</sup> Furthermore, no reports have been available for the effects of particle morphology on microstructures and electrochemical properties of crystalline sulfide electrolytes. This is due to the difficulty in controlling their morphology without loss of ionic conductivities.<sup>[20]</sup>

The aim of this study is to investigate the effects of particle size distribution of crystalline solid electrolytes on microstructures and electrochemical properties in composite cathodes. Microstructures, ionic and electronic conductivities, and charge/discharge properties were investigated when the particle size distribution of the  $\text{Li}_{10}\text{GeP}_2\text{S}_{12}$  solid electrolyte changed.

## Results and Discussion

### Fabrication and ionic conductivity of $\text{Li}_{10}\text{GeP}_2\text{S}_{12}$ with different size distributions

We first tried to control the particle size distribution of a  $\text{Li}_{10}\text{GeP}_2\text{S}_{12}$  solid electrolyte by changing the morphology of the precursor mixtures. The precursors were fabricated via a tribochemical reaction among the starting materials of  $\text{Li}_2\text{S}$ ,  $\text{GeS}_2$ , and  $\text{P}_2\text{S}_5$  using a vibration mill for 5, 30, 60, and 90 min. SEM analyses clarified that the morphology of the precursors changed with milling times (Supplemental Information S1). The particle diameters and their standard deviation decreased with increasing milling time from 5 to 60 min. The precursor milled for 60 min had the  $d_{50}$  size of 4.4  $\mu\text{m}$  and polydispersity index (PI: defined as the squares of the standard deviation from the mean Feret diameters) value of 0.30. The  $d_{50}$  size of the precursor milled for 90 min further decreased (4.1  $\mu\text{m}$ ). However, the PI value of the precursor milled for 90 min increased to 0.89. This might be because the particles milled for 90 min were more easily agglomerated than the others. After the milling process, the precursors were heated at 823 K for 8 h to crystallize into a  $\text{Li}_{10}\text{GeP}_2\text{S}_{12}$  phase. Figure 1 shows the X-ray diffraction (XRD) patterns and the SEM images of  $\text{Li}_{10}\text{GeP}_2\text{S}_{12}$  synthesized from the precursors milled for 5–90 min. The diffraction peaks of all the samples were attributed to  $\text{Li}_{10}\text{GeP}_2\text{S}_{12}$  with a space group of  $P42mc$ .<sup>[20]</sup> The peak positions of all the samples agreed with those of the previous  $\text{Li}_{10}\text{GeP}_2\text{S}_{12}$ . These results indicate that  $\text{Li}_{10}\text{GeP}_2\text{S}_{12}$  was successfully synthesized regardless of

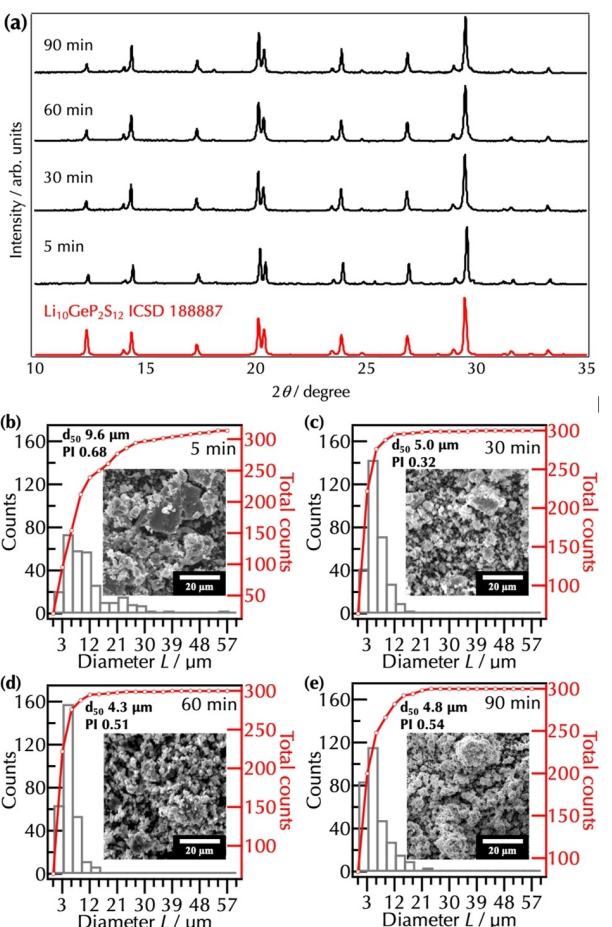


**Figure 1.** a) XRD patterns, b–e) SEM images and particle size distributions of  $\text{Li}_{10}\text{GeP}_2\text{S}_{12}$  powders synthesized from different precursors. The precursor mixtures of  $\text{Li}_2\text{S}$ ,  $\text{GeS}_2$ , and  $\text{P}_2\text{S}_5$  starting materials were prepared by vibration milling for different times of b) 5 min, c) 30 min, d) 60 min, and e) 90 min, followed by heating at 823 K for 8 h for crystallization.

the milling time. SEM image analyses revealed that the sizes of  $d_{50}$  decreased with the increase in the milling time from 5 to 60 min. The sample synthesized from the precursor milled for 60 min had a  $d_{50}$  of 4.3  $\mu\text{m}$  and the PI of 0.51, respectively. These values were like those of the corresponding precursor, indicating that the  $\text{Li}_{10}\text{GeP}_2\text{S}_{12}$  grains hardly grew during the crystallization process. However, the size of  $d_{50}$  increased by the increase in milling time from 60 min to 90 min. The size decrease up to 60 min of the milling time and the increase for 90 min agreed with the size change of the precursors in Figure S1.

Total ionic conductivities were investigated for cold-pressed  $\text{Li}_{10}\text{GeP}_2\text{S}_{12}$  pellets by electrochemical impedance spectroscopy (EIS) measurements at room temperature (Figure S2). The total ionic conductivities were 4.0–4.6  $\text{mS cm}^{-1}$ . Therefore, the average particle size of  $\text{Li}_{10}\text{GeP}_2\text{S}_{12}$  could be controlled by changing the milling time of the starting materials without losing the lithium-ion conductivity.

To fabricate  $\text{Li}_{10}\text{GeP}_2\text{S}_{12}$  powder with a small size distribution, we classified the  $\text{Li}_{10}\text{GeP}_2\text{S}_{12}$  powder by using nylon mesh sieves with 20 and 10  $\mu\text{m}$  holes. The classification with

the sieve can separate particles smaller than the hole size of the sieve from a sample powder while maintaining chemical composition and crystallinity, resulting in separation of particles larger than the hole size. We used the  $\text{Li}_{10}\text{GeP}_2\text{S}_{12}$  synthesized from the precursor milled for 60 min ( $d_{50}$ : 4.3  $\mu\text{m}$ , PI: 0.51) as a pristine  $\text{Li}_{10}\text{GeP}_2\text{S}_{12}$  (denoted as Non-60  $\text{Li}_{10}\text{GeP}_2\text{S}_{12}$ ). Figure S3 illustrates the classification process for Non-60  $\text{Li}_{10}\text{GeP}_2\text{S}_{12}$  powder. Non-60  $\text{Li}_{10}\text{GeP}_2\text{S}_{12}$  powder was first sieved through a 20  $\mu\text{m}$  sieve, and the permeated sample was further sieved through a 10  $\mu\text{m}$  sieve (class A  $\text{Li}_{10}\text{GeP}_2\text{S}_{12}$ ). The residues on the 10  $\mu\text{m}$  sieve were also collected (class B  $\text{Li}_{10}\text{GeP}_2\text{S}_{12}$ ) so as to investigate the size effects on microstructure and charge/discharge properties of composite cathodes. The XRD pattern of a  $\text{Li}_{10}\text{GeP}_2\text{S}_{12}$  structure was maintained for both class A and B  $\text{Li}_{10}\text{GeP}_2\text{S}_{12}$ , meaning that the crystal structure changed little during the classification process (Figure S4). Figure 2 shows the SEM images and particle size distributions of class A and B  $\text{Li}_{10}\text{GeP}_2\text{S}_{12}$ . Class A  $\text{Li}_{10}\text{GeP}_2\text{S}_{12}$  contained more small particles (<4  $\mu\text{m}$ ) (219 counts) than Non-60  $\text{Li}_{10}\text{GeP}_2\text{S}_{12}$  (131 counts). The  $d_{50}$  diameter and the PI value of class A  $\text{Li}_{10}\text{GeP}_2\text{S}_{12}$  were 2.8  $\mu\text{m}$  and 0.43, respectively, and smaller than those of Non-60  $\text{Li}_{10}\text{GeP}_2\text{S}_{12}$ . The coarse particles and aggregates were sufficiently removed by the classification process. In contrast, the number of the small particles (<4  $\mu\text{m}$ ) in class B  $\text{Li}_{10}\text{GeP}_2\text{S}_{12}$  (the residue on the 10  $\mu\text{m}$  sieve after classification) was 69 counts and smaller than those of class A and Non-60  $\text{Li}_{10}\text{GeP}_2\text{S}_{12}$ . The  $d_{50}$  diameter and the PI value of class B  $\text{Li}_{10}\text{GeP}_2\text{S}_{12}$  were 5.9  $\mu\text{m}$  and 0.51, respectively. Both class A and B  $\text{Li}_{10}\text{GeP}_2\text{S}_{12}$  possessed the different particle size

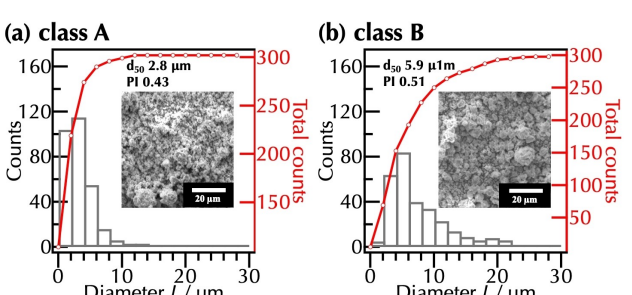


**Figure 2.** SEM images and particle size distributions of a) class A and b) class B  $\text{Li}_{10}\text{GeP}_2\text{S}_{12}$  classified from Non-60  $\text{Li}_{10}\text{GeP}_2\text{S}_{12}$  powder.

Milling time [min]	Classification	$d_{50}$ [ $\mu\text{m}$ ]	PI	Tap density $\rho$ [ $\text{g cm}^{-3}$ ]	$\sigma_{\text{total}}$ (R.T.) [ $\text{mS cm}^{-1}$ ]
5	–	9.6	0.68	1.40	4.5
30	–	5.0	0.32	1.61	4.0
60	– (Non-60)	4.3	0.51	1.68	4.6
90	–	4.8	0.54	1.49	4.4
60	Class A	2.8	0.43	1.58	1.4
60	Class B	5.9	0.52	1.54	2.3

distributions from Non-60  $\text{Li}_{10}\text{GeP}_2\text{S}_{12}$  powder. Class A and B  $\text{Li}_{10}\text{GeP}_2\text{S}_{12}$  exhibited the total ionic conductivities of 1.4 and 2.3  $\text{mS cm}^{-1}$  at room temperature, respectively. Table 1 summarizes the size distributions and the total ionic conductivities of  $\text{Li}_{10}\text{GeP}_2\text{S}_{12}$  powders with various particle size distributions. The ion conductivities of the classified samples were lower than those of all the non-classified  $\text{Li}_{10}\text{GeP}_2\text{S}_{12}$ . The XRD patterns indicated that the crystal structure and crystallinity changed little with the classification (Figure S4). All cold-pressed pellets of the samples possessed similar tap densities (approximately 1.5  $\text{g cm}^{-3}$ ) to each other (Table 1). Therefore, the classification process barely affected the physical properties of the bulk and the tap densities. The decrease in the ionic conductivity is due to an increase in the grain boundary. The classification process should have increased the ratios of small particles to all particles in any samples, resulting in the increase in the grain boundary. This increased the resistance of the total grain boundary, resulting in low ionic conductivities. To confirm this, we performed the EIS measurements at low temperature of Non-60 and class A  $\text{Li}_{10}\text{GeP}_2\text{S}_{12}$  to separate grain boundary resistance from bulk resistance (Figure S5). Figure 3 shows the temperature dependence of total, bulk, and grain boundary resistances for Li ion conduction of Non-60 and class A  $\text{Li}_{10}\text{GeP}_2\text{S}_{12}$ . Class A  $\text{Li}_{10}\text{GeP}_2\text{S}_{12}$  showed a much higher grain boundary resistance of  $1.2 \times 10^6 \Omega$  than Non-60  $\text{Li}_{10}\text{GeP}_2\text{S}_{12}$  ( $4.0 \times 10^5 \Omega$ ) at 175 K, although no significant differences were observed for the bulk resistances. Therefore, the total resistance that increased with the classification was derived from the increase in the grain boundary. Sulfide electrolytes easily ensure a sufficient contact area by cold pressing, resulting in their low grain boundary resistance. However, our results revealed that grain boundary resistances possibly affected total resistances even if sulfide electrolytes when average particle sizes of the sulfide electrolyte decrease to several micrometers. Class B  $\text{Li}_{10}\text{GeP}_2\text{S}_{12}$  exhibited a total conductivity of 2.3  $\text{mS cm}^{-1}$ , which was between Non-60 and class A  $\text{Li}_{10}\text{GeP}_2\text{S}_{12}$ . Class B  $\text{Li}_{10}\text{GeP}_2\text{S}_{12}$  included more particles with the sizes of 10–20  $\mu\text{m}$  than Non-60 and class A  $\text{Li}_{10}\text{GeP}_2\text{S}_{12}$  because Class B

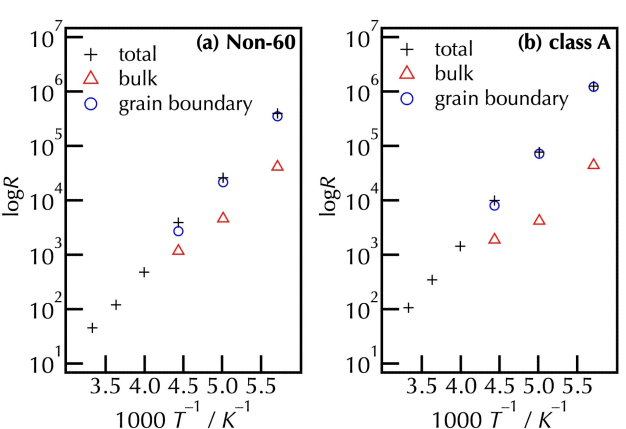


**Figure 3.** Temperature dependence of total, bulk, and grain boundary resistances for Li ion conduction of a) Non-60 and b) class A  $\text{Li}_{10}\text{GeP}_2\text{S}_{12}$ . Measurements were performed at 300–175 K.

$\text{Li}_{10}\text{GeP}_2\text{S}_{12}$  was the residue on the 10  $\mu\text{m}$  sieve after permeating through the 20  $\mu\text{m}$  sieve. The low ratios of the large particles ( $>20 \mu\text{m}$ ) and the small ( $<10 \mu\text{m}$ ) particles positively and negatively contributed to the resistance of the grain boundary, respectively. Therefore, class B  $\text{Li}_{10}\text{GeP}_2\text{S}_{12}$  with the intermediate size distribution exhibited the middle value.

Figure 4 shows the cross-sectional schematics of the ion-conductive pathways in the  $\text{Li}_{10}\text{GeP}_2\text{S}_{12}$  pellets. The key points are the grain boundaries and voids among the  $\text{Li}_{10}\text{GeP}_2\text{S}_{12}$  particles. Large particles form a few grain boundaries and large voids. In contrast, small particles form numerous grain boundaries and small voids. All non-classified  $\text{Li}_{10}\text{GeP}_2\text{S}_{12}$  pellets exhibited total ionic conductivities of 4.0–4.6  $\text{mS cm}^{-1}$  regardless of  $d_{50}$  and PI values. The non-classified  $\text{Li}_{10}\text{GeP}_2\text{S}_{12}$  pellets should have contained a few large ( $>20 \mu\text{m}$ ) and small ( $<10 \mu\text{m}$ ) particles even changing the  $d_{50}$  and PI values, because they were not classified with the sieves. The large and small particles contributed to the decrease in grain boundaries and voids, respectively, as shown in Figure 4(a). Therefore, the ionic conductivities hardly changed even when  $d_{50}$  and PI values changed. Class A and B  $\text{Li}_{10}\text{GeP}_2\text{S}_{12}$  pellets exhibited the lower ionic conductivities of 1.4 and 2.3  $\text{mS cm}^{-1}$ , respectively, than all the non-classified  $\text{Li}_{10}\text{GeP}_2\text{S}_{12}$ . Almost all the particles in class A  $\text{Li}_{10}\text{GeP}_2\text{S}_{12}$  possessed sizes smaller than 10  $\mu\text{m}$ . The small ( $<10 \mu\text{m}$ ) particles formed numerous pathways for the ionic conduction by occupation of the voids. However, the small particles also formed many grain boundaries, resulting in the low ionic conductivity, as shown in Figure 4(b). Furthermore, class B  $\text{Li}_{10}\text{GeP}_2\text{S}_{12}$  possessed less small-particles ( $<10 \mu\text{m}$ ) than class A  $\text{Li}_{10}\text{GeP}_2\text{S}_{12}$ . Therefore, the less of small particles (<

10  $\mu\text{m}$ ) increased the voids among the particles, meaning that the conductive pathways decreased, as shown in Figure 4(c). However, the grain boundaries in class B  $\text{Li}_{10}\text{GeP}_2\text{S}_{12}$  decreased, compared to class A  $\text{Li}_{10}\text{GeP}_2\text{S}_{12}$ . Thus, the ionic conductivity of class B  $\text{Li}_{10}\text{GeP}_2\text{S}_{12}$  was mid-between those of the non-classified and class A  $\text{Li}_{10}\text{GeP}_2\text{S}_{12}$ . The particle morphology of solid electrolytes has been expected to affect their ionic conductivities, but there have been no experimental reports that focused on the relationship between the morphology and the ionic conductivity of the  $\text{Li}_{10}\text{GeP}_2\text{S}_{12}$  solid electrolyte. Here, the particle size distribution significantly contributed to the Li ion conduction in the  $\text{Li}_{10}\text{GeP}_2\text{S}_{12}$  pellet. Furthermore, the large ( $>20 \mu\text{m}$ ) and small ( $<10 \mu\text{m}$ ) particles play an important role in the ionic conduction in the separator layer for all-solid-state batteries.

### Electrochemical properties of $\text{LiCoO}_2\text{-Li}_{10}\text{GeP}_2\text{S}_{12}$ cathode composites using $\text{Li}_{10}\text{GeP}_2\text{S}_{12}$ with different size distributions

The obtained  $\text{Li}_{10}\text{GeP}_2\text{S}_{12}$  particles with the various size distributions were applied to composite cathodes using  $\text{LiCoO}_2$  as the active material. The  $\text{LiCoO}_2$  particles were modified with amorphous  $\text{LiNbO}_3$  layer to decrease the ionic conduction resistance between the  $\text{LiCoO}_2$  and  $\text{Li}_{10}\text{GeP}_2\text{S}_{12}$ .<sup>[20,25,26]</sup> The  $d_{50}$  diameter and the PI value of the  $\text{LiCoO}_2$  powder were 7.3  $\mu\text{m}$  and 0.18, respectively (Figure S6). First, the ionic and electronic conductivities of the  $\text{LiCoO}_2\text{-Li}_{10}\text{GeP}_2\text{S}_{12}$  composite cathodes were investigated by DC polarization measurements using electron and ion-blocking cells. Figure 5 shows the SEM-EDX images and the ionic and electronic conductivities of the  $\text{LiCoO}_2\text{-Li}_{10}\text{GeP}_2\text{S}_{12}$  composite cathodes using Non-60, class A, and class B  $\text{Li}_{10}\text{GeP}_2\text{S}_{12}$ . The atomic distributions of O and S in the SEM-EDX images

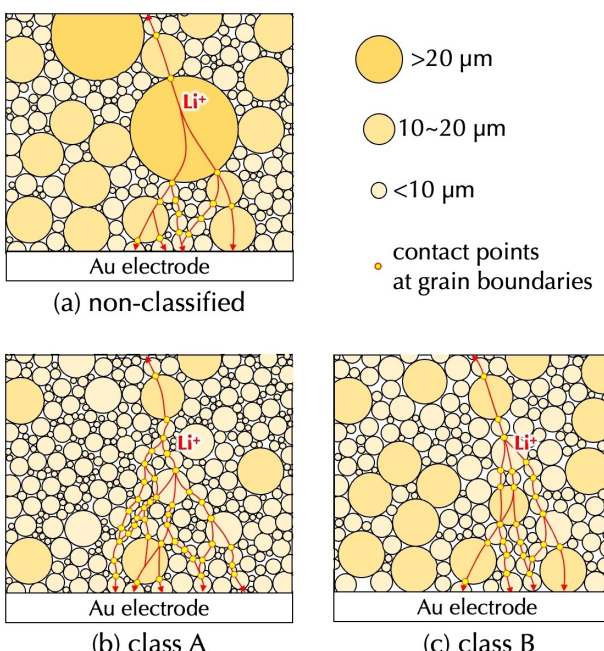


Figure 4. Schematics of cross-sectional conduction pathways for lithium ions in the cold-pressed pellets of a) non-classified, b) class A, and c) class B  $\text{Li}_{10}\text{GeP}_2\text{S}_{12}$ .

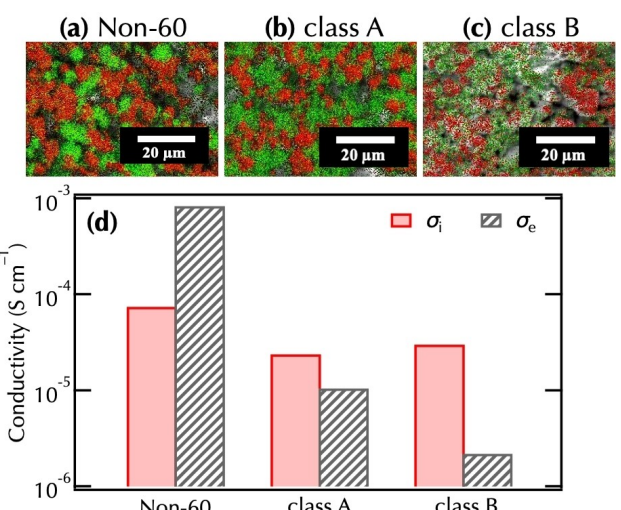
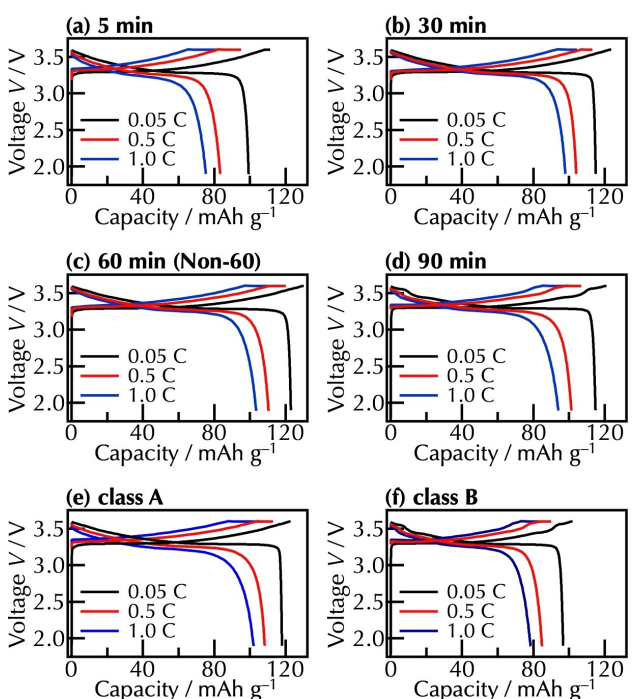


Figure 5. SEM/EDX images of  $\text{LiCoO}_2\text{-Li}_{10}\text{GeP}_2\text{S}_{12}$  composite cathodes using a) Non-60, b) class A, and c) class B  $\text{Li}_{10}\text{GeP}_2\text{S}_{12}$ . Red and green regions represent O and S atoms, respectively. (d) Ionic and electronic conductivities estimated from the DC polarization measurements using electron and ion-blocking cells. The volumetric ratios were  $\text{LiCoO}_2\text{:Li}_{10}\text{GeP}_2\text{S}_{12}=5\text{:}5$ .

correspond to the LiCoO<sub>2</sub> and Li<sub>10</sub>GeP<sub>2</sub>S<sub>12</sub> particles, respectively. All the composite cathodes comprised well-dispersed LiCoO<sub>2</sub> and Li<sub>10</sub>GeP<sub>2</sub>S<sub>12</sub>. The aggregated Li<sub>10</sub>GeP<sub>2</sub>S<sub>12</sub> was partially observed only in the composite cathode using class B Li<sub>10</sub>GeP<sub>2</sub>S<sub>12</sub>. The order of the electronic conductivities was (Non-60) > (class A) > (class B). The composite cathodes using Non-60 Li<sub>10</sub>GeP<sub>2</sub>S<sub>12</sub> exhibited especially high electronic conductivity. Non-60 Li<sub>10</sub>GeP<sub>2</sub>S<sub>12</sub> should have contained the fewest particles smaller than 10 and 20 μm among the three samples. Therefore, Non-60 Li<sub>10</sub>GeP<sub>2</sub>S<sub>12</sub> particles could not be uniformly dispersed into the voids between LiCoO<sub>2</sub> particles, resulting in the largest contact area between LiCoO<sub>2</sub> particles. The largest contact area led to the highest electronic conductivity. In contrast, the grain boundaries and voids among LiCoO<sub>2</sub> particles were uniformly and densely occupied with the Li<sub>10</sub>GeP<sub>2</sub>S<sub>12</sub> particles smaller than 10 μm in the composite cathode using class A Li<sub>10</sub>GeP<sub>2</sub>S<sub>12</sub>, resulting in the small contact area between LiCoO<sub>2</sub> particles. The small contact area caused the low electronic conductivity. With the composite cathode using class B Li<sub>10</sub>GeP<sub>2</sub>S<sub>12</sub>, the void sizes appeared to be increased compared to the composite cathode using class A Li<sub>10</sub>GeP<sub>2</sub>S<sub>12</sub> because class B Li<sub>10</sub>GeP<sub>2</sub>S<sub>12</sub> possessed larger particle sizes than class A Li<sub>10</sub>GeP<sub>2</sub>S<sub>12</sub>. Therefore, the composite cathode using class B Li<sub>10</sub>GeP<sub>2</sub>S<sub>12</sub> showed the lowest electronic conductivity. However, the ionic conductivities were not drastically different from each other, compared with the electronic conductivities. Only the composite cathode using Non-60 Li<sub>10</sub>GeP<sub>2</sub>S<sub>12</sub> exhibited a slightly higher ionic conductivity than the others. The ionic conductivities (<10<sup>-4</sup> S cm<sup>-1</sup>) were much lower than those of each Li<sub>10</sub>GeP<sub>2</sub>S<sub>12</sub> pellet (>10<sup>-3</sup> S cm<sup>-1</sup>). Therefore, all the low ionic conductivities of the composite cathodes could be due to the existence of the LiCoO<sub>2</sub> particles among the Li<sub>10</sub>GeP<sub>2</sub>S<sub>12</sub> particles. Thus, the particle size distribution affected also the electronic and ionic conductivities of the composite cathodes.

Figure 6 shows the charge/discharge curves of the LiCoO<sub>2</sub>-Li<sub>10</sub>GeP<sub>2</sub>S<sub>12</sub> composite cathodes using the Li<sub>10</sub>GeP<sub>2</sub>S<sub>12</sub> with different size distributions. All composite cathodes exhibited plateau regions at around 3.3 V (3.9 V vs. Li/Li<sup>+</sup>), corresponding to reversible Li<sup>+</sup> (de)intercalation into/from the LiCoO<sub>2</sub>.<sup>[20,25]</sup> The composite cathode using the non-classified Li<sub>10</sub>GeP<sub>2</sub>S<sub>12</sub> with the d<sub>50</sub> of 9.6 μm exhibited the discharge capacity of 99 mAh g<sup>-1</sup> at 0.05 C (Figure 6a). This discharge capacity was less than the theoretical value estimated from the cut-off voltages (approximately 130 mAh g<sup>-1</sup>). Furthermore, the discharge capacity decreased significantly to 75 mAh g<sup>-1</sup> at 1.0 C, which was 75.7% of that at 0.05 C. This suggests ion-conductive pathways were not sufficiently constructed in the composite cathode. The contact area between LiCoO<sub>2</sub> and Li<sub>10</sub>GeP<sub>2</sub>S<sub>12</sub> should have been small due to the large d<sub>50</sub> and PI values, resulting in the limitation of the Li<sup>+</sup> (de)intercalation in the composite cathode. Composite cathodes using the non-classified Li<sub>10</sub>GeP<sub>2</sub>S<sub>12</sub> with d<sub>50</sub> of 5.0 μm and 4.3 μm (Non-60) showed discharge capacities of 115 and 123 mAh g<sup>-1</sup> at 0.05 C, respectively (Figure 6b, c). The capacities at 1.0 C were 84.3%



**Figure 6.** Charge/discharge curves of LiCoO<sub>2</sub>-Li<sub>10</sub>GeP<sub>2</sub>S<sub>12</sub> composite cathodes using Li<sub>10</sub>GeP<sub>2</sub>S<sub>12</sub> with various particle size distributions. a-d) The non-classified Li<sub>10</sub>GeP<sub>2</sub>S<sub>12</sub> were synthesized from the precursors milled for a) 5, b) 30, c) 60 (Non-60), and d) 90 min. e, f) The Li<sub>10</sub>GeP<sub>2</sub>S<sub>12</sub> were classified and labeled as e) class A and f) class B. The d<sub>50</sub> and PI values of Li<sub>10</sub>GeP<sub>2</sub>S<sub>12</sub> used in the composites were a) 9.6 μm and 0.68, b) 5.0 μm and 0.32, c) 4.3 μm and 0.51, and d) 4.8 μm and 0.54, e) 2.8 μm and 0.43, f) 5.9 μm and 0.52, respectively. The volumetric ratios were LiCoO<sub>2</sub>:Li<sub>10</sub>GeP<sub>2</sub>S<sub>12</sub> = 5:5. The current densities were 0.05 C, 0.5 C, and 1.0 C (137 mA g<sup>-1</sup>).

(97 mAh g<sup>-1</sup>) and 83.7% (103 mAh g<sup>-1</sup>) compared to those at 0.05 C, respectively. The discharge capacities at 0.05 C were close to the theoretical value (approximately 130 mAh g<sup>-1</sup>) with a decrease in the d<sub>50</sub> from 9.6 to 4.3 μm. Retention ratios of discharge capacities at 1.0 C to those at 0.05 C also increased with decrease in the d<sub>50</sub>. These results suggest that the contacts between LiCoO<sub>2</sub> and Li<sub>10</sub>GeP<sub>2</sub>S<sub>12</sub> particles were improved by the small Li<sub>10</sub>GeP<sub>2</sub>S<sub>12</sub> particles. When Li<sub>10</sub>GeP<sub>2</sub>S<sub>12</sub> with a d<sub>50</sub> of 4.8 μm and the PI of 0.54 was used, the composite cathode exhibited the discharge capacities of 115, 101, and 93 mAh g<sup>-1</sup> at 0.05 C, 0.5 C, and 1.0 C, respectively (Figure 6d). The capacity at 0.05 C was the same as that of the composite cathode using Li<sub>10</sub>GeP<sub>2</sub>S<sub>12</sub> with the d<sub>50</sub> of 5.0 μm because of the d<sub>50</sub> size was similar. However, the capacity at 1.0 C was maintained at just 80.8% of that at 0.05 C. This appears due to the difference in the PI value. The Li<sub>10</sub>GeP<sub>2</sub>S<sub>12</sub> particles with d<sub>50</sub> of 4.8 μm and the PI of 0.54 partially aggregated on the SEM measurement (Figure 1d). The Li<sub>10</sub>GeP<sub>2</sub>S<sub>12</sub> aggregates did not sufficiently disperse between the LiCoO<sub>2</sub> particles, resulting in the reduction of the contact area between Li<sub>10</sub>GeP<sub>2</sub>S<sub>12</sub> and the LiCoO<sub>2</sub> in the composite cathode. The composite cathode using class A Li<sub>10</sub>GeP<sub>2</sub>S<sub>12</sub> showed a discharge capacity of 118, 108, and 102 mAh g<sup>-1</sup> at 0.05 C, 0.5 C, and 1.0 C, respectively (Figure 6e). The capacity at 0.05 C was slightly lower than the

composite cathode using Non-60  $\text{Li}_{10}\text{GeP}_2\text{S}_{12}$  ( $123 \text{ mAh g}^{-1}$ ). This is due to the difference in ionic conductivity. However, the capacity at  $1.0 \text{ C}$  kept  $86.4\%$  of that at  $0.05 \text{ C}$ , which was higher than  $83.7\%$  for Non-60  $\text{Li}_{10}\text{GeP}_2\text{S}_{12}$ . This result suggests that (de)intercalation in the composite cathode using class A  $\text{Li}_{10}\text{GeP}_2\text{S}_{12}$  occurred more easily at the interfaces between the  $\text{LiCoO}_2$  and the  $\text{Li}_{10}\text{GeP}_2\text{S}_{12}$  particles than in the composite cathode using Non-60  $\text{Li}_{10}\text{GeP}_2\text{S}_{12}$ . Class B  $\text{Li}_{10}\text{GeP}_2\text{S}_{12}$  possessed a higher ionic conductivity than Class A  $\text{Li}_{10}\text{GeP}_2\text{S}_{12}$ . However, the composite cathode using class B  $\text{Li}_{10}\text{GeP}_2\text{S}_{12}$  exhibited smaller discharge capacities at all C rates (Figure 6f) and the lower retention ratio ( $81.2\%$ ) of capacity than the composite cathode using class A  $\text{Li}_{10}\text{GeP}_2\text{S}_{12}$ . These results suggest that small ( $<10 \mu\text{m}$ ) particles in class A  $\text{Li}_{10}\text{GeP}_2\text{S}_{12}$  positively contributed to the ionic conduction in the composite cathodes by occupying large and small voids among  $\text{LiCoO}_2$  particles. Therefore, the particle size distribution of the solid  $\text{Li}_{10}\text{GeP}_2\text{S}_{12}$  electrolyte drastically contributed to the capacity and reaction rate of the composite cathode. The order of the capacities of the composite cathodes using Non-60, class A, and class B  $\text{Li}_{10}\text{GeP}_2\text{S}_{12}$  at each C rate agreed with that of the electronic conductivities in Figure 5. Low electronic conductivity means the existence of localized  $\text{LiCoO}_2$  particles. The localized  $\text{LiCoO}_2$  cannot give and receive electrons, leading to an insufficient proceeding of the (de)intercalation. Therefore, the capacities depended on the electronic conductivities. No relationships were confirmed between the capacities, nor the retention ratios, and the ionic conductivities in Figure 5. This result suggests that the microstructures of the composite cathodes more largely affected the charge/discharge properties than the ionic conductivities measured between the two Au-electrodes.

### Effects of volumetric ratios on electrochemical properties of $\text{LiCoO}_2\text{-Li}_{10}\text{GeP}_2\text{S}_{12}$ using $\text{Li}_{10}\text{GeP}_2\text{S}_{12}$ with different size distributions

It has been strongly desired to increase the ratio of an active material to a solid electrolyte for the development of a composite cathode with a high energy density. We investigated the effects of the particle size distribution of  $\text{Li}_{10}\text{GeP}_2\text{S}_{12}$  on the suitable volumetric ratio of  $\text{LiCoO}_2$  to  $\text{Li}_{10}\text{GeP}_2\text{S}_{12}$  in the composite cathodes. Figure 7 shows the cross-sectional SEM-EDX images, and electronic and ionic conductivities of the  $\text{LiCoO}_2\text{-Li}_{10}\text{GeP}_2\text{S}_{12}$  composite cathodes with various volumetric ratios of  $\text{LiCoO}_2$  to  $\text{Li}_{10}\text{GeP}_2\text{S}_{12}$  (5:5, 7:3, 8:2, and 9:1). Non-60 and class A  $\text{Li}_{10}\text{GeP}_2\text{S}_{12}$  were applied to the composite cathodes, which are denoted as LCO-LGPS(N60/A;  $x:10-x$ ). In the SEM-EDX images, the area where oxygen was detected expanded with increasing volumetric ratio of  $\text{LiCoO}_2$  for both composites. Class A  $\text{Li}_{10}\text{GeP}_2\text{S}_{12}$  tended to disperse more uniformly than Non-60  $\text{Li}_{10}\text{GeP}_2\text{S}_{12}$ . In the composite cathodes, one kind of the particles should have surrounded the other kind of the particles, and hence one kind of the particles interrupted the electron- and ion-conductive pathways between the other kind of the particles. The electronic and ionic conductivities of the composite cathodes were derived mainly from the  $\text{LiCoO}_2$  and the  $\text{Li}_{10}\text{GeP}_2\text{S}_{12}$ , respectively. Both the ionic conductivities of the composite cathodes increased with increasing ratios of each  $\text{Li}_{10}\text{GeP}_2\text{S}_{12}$ . The ionic conductivities of LCO-LGPS(A) were lower than those of LCO-LGPS(N60). The electronic conductivities of LCO-LGPS(A) obviously increased with the increase in the  $\text{LiCoO}_2$  ratio, whereas those of LCO-LGPS(N60) slightly increased. Class A  $\text{Li}_{10}\text{GeP}_2\text{S}_{12}$  uniformly dispersed into the interfaces between the  $\text{LiCoO}_2$  particles because it consisted mainly of small ( $<10 \mu\text{m}$ ) particles. Therefore, the ionic and electronic conductivities derived from class A  $\text{Li}_{10}\text{GeP}_2\text{S}_{12}$  and  $\text{LiCoO}_2$  were interrupted with increasing ratio of  $\text{LiCoO}_2$  and

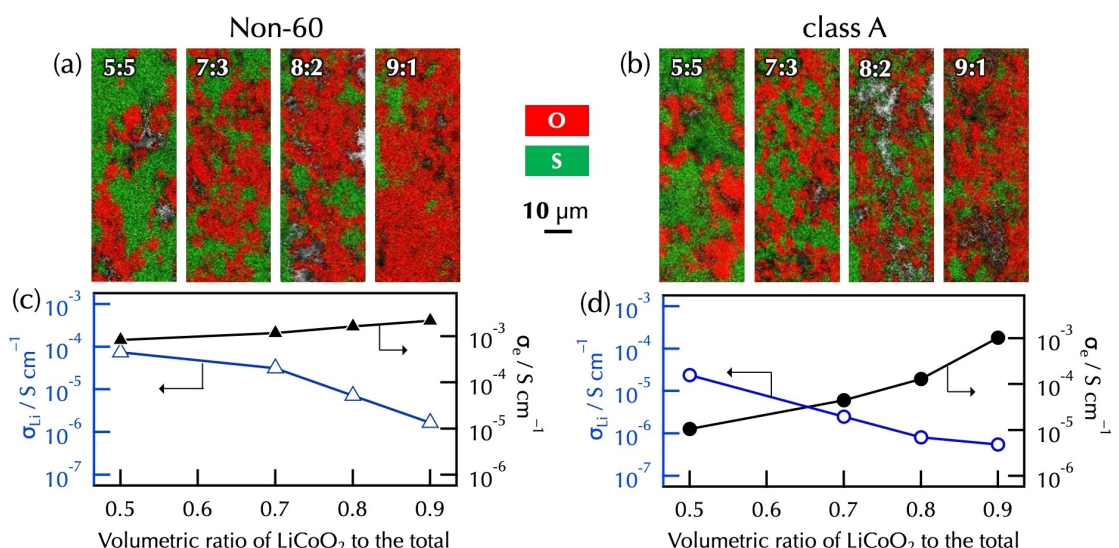


**Figure 7.** a, b) Cross-sectional SEM-EDX images and c, d) electronic and ionic conductivities of the  $\text{LiCoO}_2\text{-Li}_{10}\text{GeP}_2\text{S}_{12}$  composites with different volume ratios of  $\text{LiCoO}_2$  to  $\text{Li}_{10}\text{GeP}_2\text{S}_{12}$  (5:5, 7:3, 8:2, and 9:1). a, c) Non-60 and b, d) class A  $\text{Li}_{10}\text{GeP}_2\text{S}_{12}$  were used in the composite cathodes. Typical DC polarization curves are shown in Figure S7.

class A  $\text{Li}_{10}\text{GeP}_2\text{S}_{12}$ , respectively. However, Non-60  $\text{Li}_{10}\text{GeP}_2\text{S}_{12}$  appeared to not uniformly disperse into the interfaces between  $\text{LiCoO}_2$  particles compared to class A  $\text{Li}_{10}\text{GeP}_2\text{S}_{12}$ , because Non-60  $\text{Li}_{10}\text{GeP}_2\text{S}_{12}$  included large ( $> 20 \mu\text{m}$ ) particles. This is why the both ionic and electronic conductivities of LCO-LGPS(N60) were higher than those of LCO-LGPS(A) regardless of the volumetric ratios. These results also suggest that the microstructure in the composite cathodes drastically affected their electrochemical properties.

Figure 8 shows the charge/discharge curves and summarized capacity retentions of LCO-LGPS(N60/A;  $x:10-x$ ) with various volumetric ratios of  $x=5, 7, 8$ , and  $9$ . The charge/discharge measurements were conducted for five cycles at each current density of  $0.05, 0.1, 0.5$ , and  $1.0 \text{ C}$ . The charge/discharge capacities of LCO-LGPS(N60) decreased with increasing volumetric ratios of  $\text{LiCoO}_2$ . This revealed that the (de)intercalation sites and the ion-conductive pathways decreased by the decreases in the interfaces between  $\text{LiCoO}_2$ - $\text{Li}_{10}\text{GeP}_2\text{S}_{12}$  particles and  $\text{Li}_{10}\text{GeP}_2\text{S}_{12}$ - $\text{Li}_{10}\text{GeP}_2\text{S}_{12}$ , respectively. The Coulombic effi-

cies of the first charge/discharge capacities at  $0.05 \text{ C}$  were  $95.3\%$ ,  $85.3\%$ ,  $74.5\%$  and  $58.5\%$  for LCO-LGPS(N60) with the volumetric ratios of  $5:5$ ,  $7:3$ ,  $8:2$ , and  $9:1$ , respectively. The charge/discharge capacities of LCO-LGPS(N60) gradually decreased with the cycle numbers regardless of the volumetric ratios. Thus, some  $\text{LiCoO}_2$  particles were electrochemically deactivated during cycling when the volumetric ratios of  $\text{LiCoO}_2$  to  $\text{Li}_{10}\text{GeP}_2\text{S}_{12}$  were equal or greater than  $5:5$ . Considering that the capacities mainly decreased at the discharge processes, the decrease in capacity was due to losing physical contacts between  $\text{LiCoO}_2$  and  $\text{Li}_{10}\text{GeP}_2\text{S}_{12}$  particles, which was caused by the decrease in the volume of  $\text{LiCoO}_2$  particles due to intercalation of Li ions in the discharge processes.<sup>[27]</sup> The decrease in the discharge capacity of LCO-LGPS(N60) became notable with the increase in the C rate when the volumetric ratios were  $7:3$ ,  $8:2$ , and  $9:1$ . The poor rate capability also suggests that the decrease in the contact area between the  $\text{LiCoO}_2$  and  $\text{Li}_{10}\text{GeP}_2\text{S}_{12}$  particles caused the increase in apparent reaction resistance.

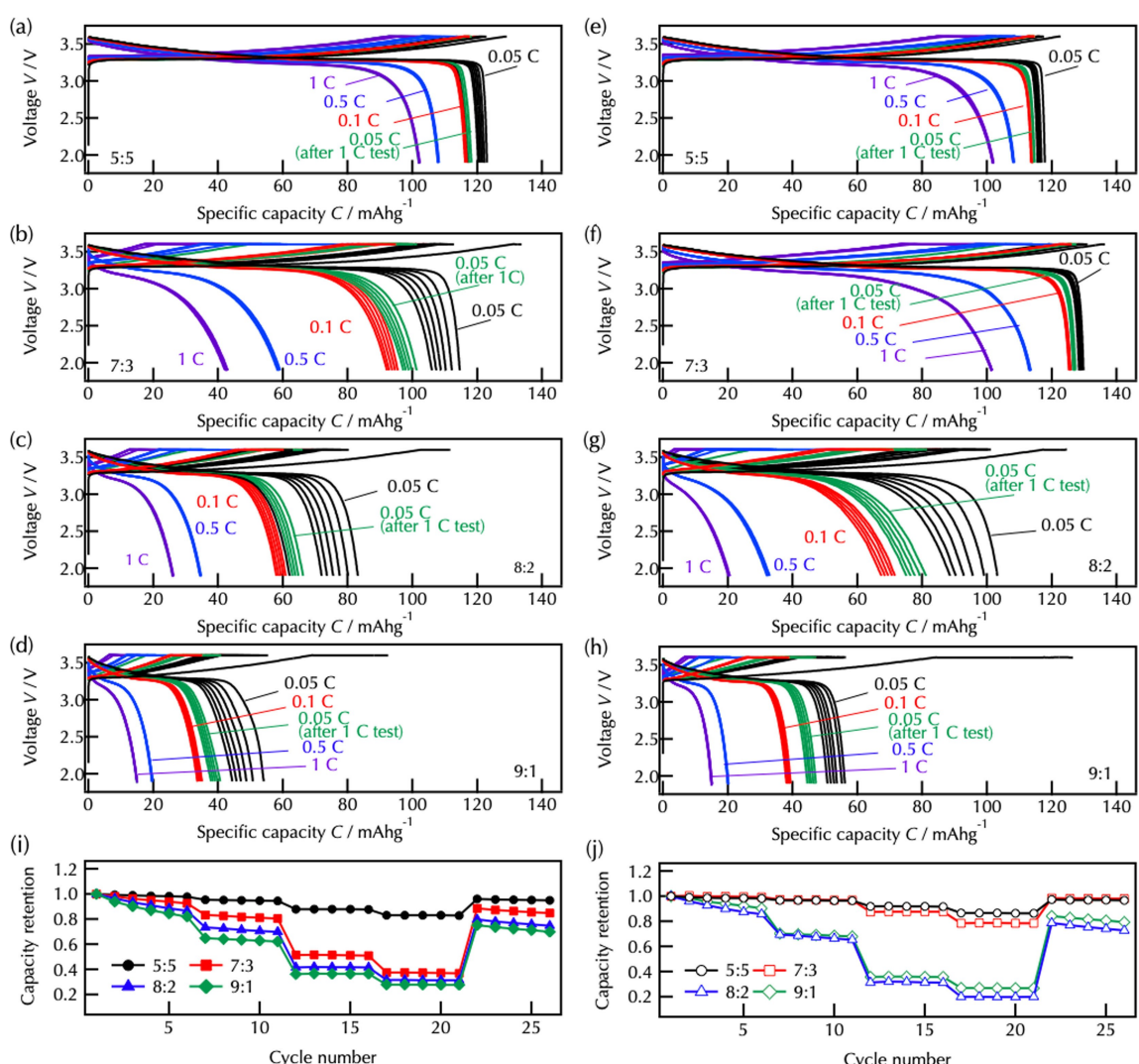


**Figure 8.** a-h) Charge/discharge curves and i, j) summarized capacity retentions of  $\text{LiCoO}_2$ - $\text{Li}_{10}\text{GeP}_2\text{S}_{12}$  cathode composites with various volumetric ratios of  $\text{LiCoO}_2$  to  $\text{Li}_{10}\text{GeP}_2\text{S}_{12}$  of a, e)  $5:5$ , b, f)  $7:3$ , c, g)  $8:2$ , and d, h)  $9:1$ . a-d, i) (Non-60) and e-h, j) class A  $\text{Li}_{10}\text{GeP}_2\text{S}_{12}$  were used. The current densities were  $0.05 \text{ C}$ ,  $0.1 \text{ C}$ ,  $0.5 \text{ C}$ , and  $1 \text{ C}$ .

LCO-LGPS(A; 7:3) showed a slightly higher discharge capacity of  $129 \text{ mAh g}^{-1}$  at  $0.05 \text{ C}$  than LCO-LGPS(A; 5:5) ( $122 \text{ mAh g}^{-1}$ ). LCO-LGPS(A; 7:3) showed a discharge capacity of  $126 \text{ mAh g}^{-1}$  at the 26th cycle (after the rate test), resulting in the retention ratio of 98.0% (26th) to that at the 1st cycle. The retention ratio was slightly higher than LCO-LGPS(A; 5:5) (96.7%). The improvement in capacity at  $0.05 \text{ C}$  and the retention ratio were never confirmed on LCO-LGPS(N60). The improvement should be due to the microstructure in LCO-LGPS(A), which was uniformly mixed in Figure 7. The physical contacts between the  $\text{LiCoO}_2$  and  $\text{Li}_{10}\text{GeP}_2\text{S}_{12}$  particles were maintained by the small ( $< 10 \mu\text{m}$ )  $\text{Li}_{10}\text{GeP}_2\text{S}_{12}$  during the cycles even the volumetric ratio of  $\text{LiCoO}_2$  to the  $\text{Li}_{10}\text{GeP}_2\text{S}_{12}$  changed to 7:3 from 5:5. LCO-LGPS(A; 7:3) exhibited 78.4% of the retention ratio of the capacity at  $1.0 \text{ C}$  to that at  $0.05 \text{ C}$ , which was lower than those of LCO-LGPS(N60; 5:5) and LCO-LGPS(A; 5:5) (83.0% and 86.5%, respectively). This is because the contact area between  $\text{LiCoO}_2$  and  $\text{Li}_{10}\text{GeP}_2\text{S}_{12}$  particles decreased with the decrease in the volumetric ratio of  $\text{Li}_{10}\text{GeP}_2\text{S}_{12}$ . LCO-LGPS(A; 8:2 and 9:1) showed similarly poor rate capabilities, which was derived from the decrease in the contact area between  $\text{LiCoO}_2$  and  $\text{Li}_{10}\text{GeP}_2\text{S}_{12}$  particles, to LCO-LGPS(N60; 8:2 and 9:1). Furthermore, whereas the first charge capacities of LCO-LGPS(N60) decreased with decreasing volumetric ratio of the  $\text{Li}_{10}\text{GeP}_2\text{S}_{12}$ , those of LCO-LGPS(A) hardly decreased. This result also suggests that  $\text{LiCoO}_2$  and  $\text{Li}_{10}\text{GeP}_2\text{S}_{12}$  particles were uniformly mixed and dispersed in LCO-LGPS(A). However, the first discharge caused the decrease in the volume of  $\text{LiCoO}_2$  and following the decrease in contact areas between  $\text{LiCoO}_2$  and the  $\text{Li}_{10}\text{GeP}_2\text{S}_{12}$  particles. Therefore, the capacities of LCO-LGPS(A; 8:2 and 9:1) decreased drastically after the first charge. It is notable that the electronic and ionic conductivities in Figure 7 cannot completely explain the drastic decrease in the rate capability of LCO-LGPS(A; 8:2 and 9:1) by the increase in the ratio of  $\text{LiCoO}_2$  from 7:3 to 8:2. The drastic decrease is explained by focusing on the microstructure in the next section.

#### Conduction pathways for electron and lithium ion and effective contact area in $\text{LiCoO}_2$ - $\text{Li}_{10}\text{GeP}_2\text{S}_{12}$ composites

(De)intercalation sites, electron-conductive pathways, ion-conductive pathways, and their balance must be sufficiently ensured to establish composite cathodes with high energy and high power densities. The (de)intercalation sites, electron-conductive pathways, and ion-conductive pathways should correspond to the interfaces between particles of AM-SE, AM-AM, and SE-SE, respectively (AM: active material, SE: solid electrolyte). Therefore, adjustment of the balance of interface areas among AM-SE, AM-AM, and SE-SE is required. Figure 9 shows the schematics of LCO-LGPS(N60; 7:3) and LCO-LGPS(A).

In the case of LCO-LGPS(N60; 7:3),  $\text{LiCoO}_2$  and  $\text{Li}_{10}\text{GeP}_2\text{S}_{12}$  were not uniformly mixed because of the large ( $> 20 \mu\text{m}$ ) and a few small ( $< 10 \mu\text{m}$ ) particles, leading to sufficient pathways for electronic and ionic conductions in the inter-electrode direction (Figure 9a). Thus, the electronic and ionic conductivities observed by electrochemical measurements showed no signifi-

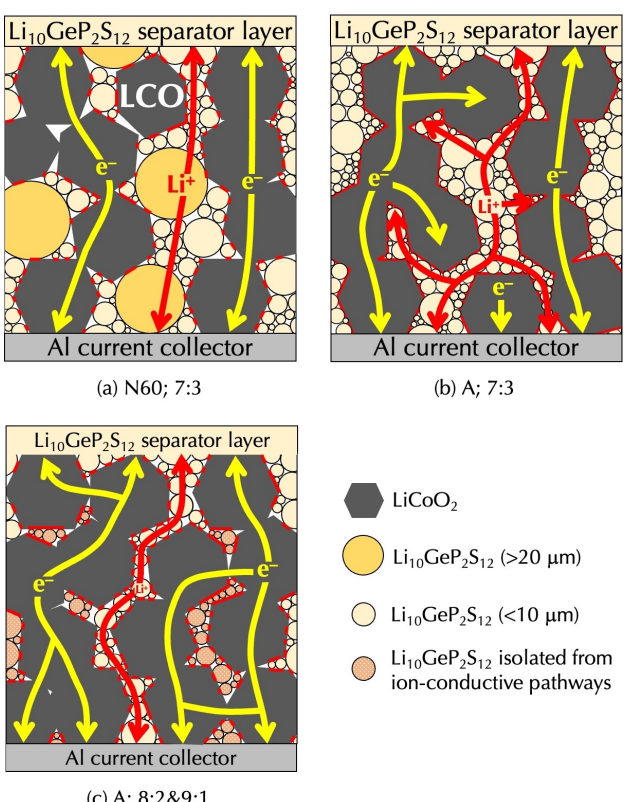


**Figure 9.** Schematics of cross-sectional conduction pathways for electrons and  $\text{Li}$  ions in LCO-LGPS with various volume ratios of  $\text{LiCoO}_2$  to  $\text{Li}_{10}\text{GeP}_2\text{S}_{12}$ : a) N60; 7:3; b) A; 7:3, and c) A; 8:2 and 9:1.

cant changes when the volumetric ratio of  $\text{LiCoO}_2$  increased from 0.5 to 0.7 (Figure 7c). However, the interfacial area between  $\text{LiCoO}_2$  and  $\text{Li}_{10}\text{GeP}_2\text{S}_{12}$  should be small due to the insufficient mixing condition. This limited the rate of lithium (de)intercalation at the  $\text{LiCoO}_2/\text{Li}_{10}\text{GeP}_2\text{S}_{12}$  interfaces. Then, LCO-LGPS(N60; 7:3) exhibited the much lower rate capability than LCO-LGPS(N60; 5:5) (Figure 8a, b). Furthermore, the insufficient mixing condition caused some  $\text{LiCoO}_2$  particles isolated from the electronic conduction pathways, which could be associated with the small discharge capacity observed at the low current density of  $0.05 \text{ C}$ .

The charge/discharge capacities and capacity retentions of LCO-LGPS(A; 7:3) were higher than those of LCO-LGPS(N60; 5:5) even the both ionic and electronic conductivities of LCO-LGPS(A; 7:3) were lower than those of LCO-LGPS(N60; 7:3). The microstructure is the key point to explain this phenomenon. The interface areas of AM-SE and SE-SE in LCO-LGPS(A) were more sufficiently ensured and kept during the charge/discharge cycles than those of in LCO-LGPS(N60) by occupying the voids with the small ( $< 10 \mu\text{m}$ ) particles existing uniformly. This suggests that the (de)intercalation sites and conductive pathways were three-dimensionally formed, as shown in Figure 9(b). This is why the LCO-LGPS(A 7:3) showed the high charge/discharge capacities and capacity retentions. The three-dimensional information was not able to be clarified by the DC

polarization measurements because they captured just the one-dimensional information between the 2 electrodes.

LCO-LGPS(A; 8:2 and 9:1) exhibited the drastically low rate capability and capacity retentions compared with LCO-LGPS(A; 5:5 and 7:3) even the ionic conductivities did not drastically decrease in the DC polarization measurements. The electron- and ion-conductive pathways were at least one-dimensionally ensured between AM-AM and SE-SE particles as suggested in Figure 9(c). Furthermore, the essential interface areas of AM-SE in LCO-LGPS(A; 8:2 and 9:1) seemed to be ensured at the beginning stage because the first charge capacities were similar to those of LCO-LGPS(A; 5:5 and 7:3). This is due to the small ( $< 10 \mu\text{m}$ )  $\text{Li}_{10}\text{GeP}_2\text{S}_{12}$  particles, which dispersed uniformly well into the interfaces between the  $\text{LiCoO}_2$  particles. However, the first charge curve shifted to high voltages with decreasing the ratio of  $\text{Li}_{10}\text{GeP}_2\text{S}_{12}$  to 0.2 and 0.1. The active  $\text{LiCoO}_2/\text{Li}_{10}\text{GeP}_2\text{S}_{12}$  interfaces decreased by the increase in the  $\text{Li}_{10}\text{GeP}_2\text{S}_{12}$  isolated from the ion-conductive pathways due to the low volumetric ratio of  $\text{Li}_{10}\text{GeP}_2\text{S}_{12}$  (Figure 9c). Moreover, the volumetric change of  $\text{LiCoO}_2$  during the first charge/discharge additionally generated of the isolated  $\text{Li}_{10}\text{GeP}_2\text{S}_{12}$ , resulting in the loss of the (de)intercalation sites and the disconnection of the three-dimensional ion-conductive pathways. Therefore, the capacities drastically decreased after the first charge in LCO-LGPS(A; 8:2 and 9:1). Our findings demonstrate that the interfacial area between AM and SE and the continuous conductive pathways between SE and SE are the critical factors determining the capacity and rate of  $\text{LiCoO}_2\text{-Li}_{10}\text{GeP}_2\text{S}_{12}$ . Downsizing SE particles is effective to fabricate the large interfacial area and the continuous conduction pathways in the composite electrode, even if the total ionic conductivity is sacrificed a little due to increase in the grain boundary resistance. The most sufficient electron-conductive pathways, ion-conductive pathways, and (de)intercalation sites were three-dimensionally ensured and kept in LCO-LGPS(A; 7:3) by the microstructure control with the small ( $< 10 \mu\text{m}$ ) particles, among all the composite cathodes. Then, the volumetric ratio of the active material was successfully increased from 50% to 70% by control of the microstructure in the composite cathode, using the small particles of the solid electrolyte with small size distribution. When a highly ion-conductive SE is composed in the composite cathodes, their discharge properties are governed by the physical contact (microstructure), not by the ionic conductivity of SE itself.

## Conclusions

The  $\text{Li}_{10}\text{GeP}_2\text{S}_{12}$  with various particle size distribution were obtained by milling and classifying. The ionic conductivities of the obtained  $\text{Li}_{10}\text{GeP}_2\text{S}_{12}$  changed little with the changes in the  $d_{50}$  and PI values when the samples included the particles with various sizes. In the case of the  $\text{Li}_{10}\text{GeP}_2\text{S}_{12}$  classified with the sieves, the ionic conductivities depended on the particle size distribution. Small particles increased the ion-conductive pathways. Large particles decreased the resistance to the grain boundary.

The size distribution of  $\text{Li}_{10}\text{GeP}_2\text{S}_{12}$  particles affected also the charge/discharge properties of the composite cathodes. The optimum ratio of the active material was increased from 50% to 70% in volume, resulting in the improvement of the ASSB properties. Small  $\text{Li}_{10}\text{GeP}_2\text{S}_{12}$  particles ( $< 10 \mu\text{m}$ ) were especially effective in the charge/discharge properties because they were able to form three-dimensionally the (de)intercalation sites and ion-conductive pathways with suppressing interruption of the electronic conduction. The three-dimensional information was not obtained by the DC polarization measurements.

In this study, we successfully controlled the microstructure in the composite cathode by adjusting the size distribution of the solid electrolyte particles. The microstructure control led to the three-dimensional control of the balance among the electron-conductive pathways, the ion-conductive pathways, and the (de)intercalation sites. Therefore, microstructure should be controlled even if total ionic/electronic conductivities are sacrificed a little when utilizing a solid electrolyte with a sufficiently high ionic conductivity for a composite electrode. ASSB properties will be further improved by control of microstructures in composite electrodes.

## Experimental Section

### Synthesis of $\text{Li}_{10}\text{GeP}_2\text{S}_{12}$ with various size distributions

$\text{Li}_{10}\text{GeP}_2\text{S}_{12}$  was synthesized by a solid-state reaction via a mechanochemical process using a vibrating mill.<sup>[20,25]</sup>  $\text{Li}_2\text{S}$  (Mitsuba Chemical; >99.9%),  $\text{P}_2\text{S}_5$  (Sigma-Aldrich; >99%), and  $\text{GeS}_2$  (Kojundo Chemical; >99.9%) were weighed in predetermined ratios and ground with pestle in an agate mortar for 15 min. Then, 2 g of the precursor was placed in a 10 mL volume vibrating mill pot. These operations were conducted in a glove box filled with Ar to prevent exposure to atmosphere and maintain a dew point environment of less than 193 K. The mechanochemical treatment was conducted with a vibration mill (Hi-speed Vibration Sample Mill TI-100; CMT) using cylindrical rods as the milling media at 1440 rpm and 7 mm amplitude. The milling times were set to 5, 30, 60, and 90 min to change the particle size distributions. After milling, each sample was cold pressed into pellets under 180 MPa pressure. The pellets were sealed in Pyrex tubes in a 10 Pa environment and heated at 823 K for 8 h.  $\text{Li}_{10}\text{GeP}_2\text{S}_{12}$  synthesized from the raw-materials mixture milled for 60 min was classified to obtain small particles. The  $\text{Li}_{10}\text{GeP}_2\text{S}_{12}$  powder was ground in an agate mortar under Ar atmosphere for 30 min and dried at 393 K for 1 h under vacuum. The dried powder was sieved through 20 and 10  $\mu\text{m}$  nylon mesh. We collected the two powders: (class A) the powder permeated both the 20 and 10  $\mu\text{m}$  sieve and (class B) the powder permeated through the 20  $\mu\text{m}$  sieve, which remained on the 10  $\mu\text{m}$  sieve.

### Fabrication of $\text{LiCoO}_2\text{-Li}_{10}\text{GeP}_2\text{S}_{12}$ cathode composites

The  $\text{LiCoO}_2\text{-Li}_{10}\text{GeP}_2\text{S}_{12}$  cathode composites were manufactured using  $\text{Li}_{10}\text{GeP}_2\text{S}_{12}$  powders with various size distributions. A commercialized  $\text{LiCoO}_2$  powder (Nippon Chemical Industry; C-5H, average diameter: 7.96  $\mu\text{m}$ ) was used, and the  $\text{LiCoO}_2$  surface was coated with amorphous  $\text{LiNbO}_3$  using a spray coating method.<sup>[20,25,26]</sup> The composite cathodes were synthesized using a previously reported procedure.<sup>[25]</sup> The weight ratio of  $\text{LiCoO}_2$  to  $\text{Li}_{10}\text{GeP}_2\text{S}_{12}$  was 70:30, 84:16, 90:10, and 95:5, which correspond to

the volumetric ratio of 50:50, 70:30, 80:20, and 90:10, respectively.

### Structural characterization

XRD patterns of the  $\text{Li}_{10}\text{GeP}_2\text{S}_{12}$  samples were acquired with an X-ray powder diffractometer (Rigaku; SmartLab) using  $\text{Cu K}_{\alpha 1}$  radiation. The diffraction data were collected with a step width of  $0.01^\circ$  over a  $2\theta$  range  $10^\circ$ – $35^\circ$ . The morphology and atomic distribution of the  $\text{Li}_{10}\text{GeP}_2\text{S}_{12}$  samples and the  $\text{LiCoO}_2$ - $\text{Li}_{10}\text{GeP}_2\text{S}_{12}$  cathode composites were observed using a scanning electron microscope with energy dispersive X-ray spectroscope (SEM-EDX) (JEOL; JSM6610LV-JED2300). All samples were transferred from an Ar-filled glovebox to the SEM chamber using an airtight transfer cell. The particle sizes were analyzed by measuring the horizontal Feret diameters for 300 particles per field of view in the SEM images. The Feret diameter was defined as the shortest length between parallel tangent lines drawn in a certain direction at both ends of the measured particle. When the particle was agglomerated, the size of the secondary particle was measured as a single unit, which was assumed to behave like a primary particle. Particle size distributions were estimated as PI, which were defined as the squares of the standard deviation from the mean Feret diameters.

### Alternating-current (AC) electrochemical impedance spectroscopy (EIS) for $\text{Li}_{10}\text{GeP}_2\text{S}_{12}$

The ionic conductivity of  $\text{Li}_{10}\text{GeP}_2\text{S}_{12}$  was measured by AC EIS. Ion-blocking cells comprising  $\text{Au}/\text{Li}_{10}\text{GeP}_2\text{S}_{12}/\text{Au}$  were prepared under 355 MPa. The diameter and thickness of the compressed powders  $\text{Li}_{10}\text{GeP}_2\text{S}_{12}$  were 10 mm and 1–2 mm, respectively. The cell remained to be pressed under 100 MPa during the EIS measurement. Total ion conductivity was measured at room temperature with an amplitude of 10 mV and frequency sweep from 100 kHz to 100 Hz using a frequency response analyzer (Solartron Analytical; 1260). To separate the bulk resistances from intergranular resistances in the  $\text{Li}_{10}\text{GeP}_2\text{S}_{12}$  samples with various size distributions, the EIS measurements were also conducted at low temperatures from 300 to 175 K using a cryostat (Toyo Technica; LN-Z2-HF), an impedance measurement system (Keysight; Model E4990), and a temperature controller (Lake Shore; Model 336 Temperature Controller.). The frequency range was from 100 MHz to 20 Hz.

### Electrochemical characterization of $\text{LiCoO}_2$ - $\text{Li}_{10}\text{GeP}_2\text{S}_{12}$ composite cathodes

Two-electrode all-solid-state batteries of  $\text{LiCoO}_2$ - $\text{Li}_{10}\text{GeP}_2\text{S}_{12}$ / $\text{Li}_{10}\text{GeP}_2\text{S}_{12}$ /In-Li were used to investigate the electrochemical properties of the  $\text{LiCoO}_2$ - $\text{Li}_{10}\text{GeP}_2\text{S}_{12}$  composite electrodes.<sup>[25]</sup> Charge/discharge measurements were performed at 298 K with applied current rates of  $7 \text{ mA g}^{-1}$  (0.05 C) to  $140 \text{ mA g}^{-1}$  (1.0 C) using a multi-channel potentiogalvanostat (Toyo system; TOSCAT-3100). The upper and lower cut-off voltages were 3.6 and 1.9 V, respectively. Charging and discharging were conducted in a constant current constant voltage (CCCV) mode, and the CV process was terminated when the current decayed to 1/10 of the constant current value.

Direct-current (DC) polarization measurements were conducted to investigate electronic and ionic conductivities of the  $\text{LiCoO}_2$ - $\text{Li}_{10}\text{GeP}_2\text{S}_{12}$  composites.<sup>[18,28]</sup> An electron-blocking cell of In-Li/ $\text{Li}_{10}\text{GeP}_2\text{S}_{12}$ / $\text{LiCoO}_2$ - $\text{Li}_{10}\text{GeP}_2\text{S}_{12}$ / $\text{Li}_{10}\text{GeP}_2\text{S}_{12}$ /In-Li and an ion-blocking cell of  $\text{Au}/\text{LiCoO}_2$ - $\text{Li}_{10}\text{GeP}_2\text{S}_{12}/\text{Au}$  were used for the ionic and the electronic conductivity measurements, respectively. The applied voltages ranged from 0.05 to 1.0 V. The current values were

recorded after the current decayed sufficiently. Then, the resistance was estimated from the applied voltage and the recorded current.

An EIS measurement was also performed using a frequency response analyzer (Biologic; VP-300) equipped with a potentiostat to evaluate the internal resistance of a battery. The impedance of the battery was measured with the amplitude of 10 mV and the frequency sweeping from  $7 \times 10^5$  Hz to 0.01 Hz at room temperature (298 K) while maintaining the potential which made the battery 50% of the discharge capacity value (State of Charge [SOC] 50%).

### Acknowledgements

This study was partially supported by a Grant-in-Aid for Scientific Research on Innovative Areas (No. 19H05793) from the Japan Society for the Promotion of Science. We would like to thank Mr. Yohei Hasegawa for his kind assistance in charge/discharge measurements.

### Conflict of Interests

The authors declare no conflict of interest.

### Data Availability Statement

Research data are not shared.

**Keywords:** all-solid-state battery • composite cathode • microstructure • particle size distribution • ionic conductor

- [1] J. Janek, W. G. Zeier, *Nat. Energy* **2016**, *1*, 1.
- [2] S. P. Culver, R. Koerver, T. Krauskopf, W. G. Zeier, *Chem. Mater.* **2018**, *30*, 4179.
- [3] T. Tamprakis, P. Canepa, J. A. Dawson, M. S. Islam, C. Masquelier, *Nat. Mater.* **2019**, *18*, 1278.
- [4] X. Bai, Y. Duan, W. Zhuang, R. Yang, J. Wang, *J. Mater. Chem. A* **2020**, *8*, 25663.
- [5] Y. Kato, S. Hori, T. Saito, K. Suzuki, M. Hirayama, A. Mitsui, M. Yonemura, H. Iba, R. Kanno, *Nat. Energy* **2016**, *1*, 1.
- [6] W. Zhang, D. A. Weber, H. Weigand, T. Arlt, I. Manke, D. Schröder, R. Koerver, T. Leichtweiss, P. Hartmann, W. G. Zeier, J. Janek, *ACS Appl. Mater. Interfaces* **2017**, *9*, 17835.
- [7] Y. Kato, S. Shiotani, K. Morita, K. Suzuki, M. Hirayama, R. Kanno, *J. Phys. Chem. Lett.* **2018**, *9*, 607.
- [8] Y. Li, S. Daikuhara, S. Hori, X. Sun, K. Suzuki, M. Hirayama, R. Kanno, *Chem. Mater.* **2020**, *32*, 8860.
- [9] A. Bielefeld, D. A. Weber, J. Janek, *J. Phys. Chem. C* **2019**, *123*, 1626.
- [10] D. S. McLachlan, M. Blaszkiewicz, R. E. Newnham, *J. Am. Ceram. Soc.* **1990**, *73*, 2187.
- [11] N. F. Uvarov, V. P. Isupov, V. Sharma, A. K. Shukla, *Solid State Ionics* **1992**, *51*, 41.
- [12] C. M. Mari, G. Dotelli, *J. Mater. Sci.* **2001**, *36*, 1141.
- [13] L. C. R. Schneider, C. L. Martin, Y. Bultel, D. Bouvard, E. Siebert, *Electrochim. Acta* **2006**, *52*, 314.
- [14] L. C. R. Schneider, C. L. Martin, Y. Bultel, L. Dessemond, D. Bouvard, *Electrochim. Acta* **2007**, *52*, 3190.
- [15] D. Chen, L. Lu, J. Li, Z. Yu, W. Kong, H. Zhu, *J. Power Sources* **2011**, *196*, 3178.
- [16] F. Strauss, T. Bartsch, L. de Biasi, A.-Y. Kim, J. Janek, P. Hartmann, T. Brezesinski, *ACS Energy Lett.* **2018**, *3*, 992.
- [17] A. Sakuda, T. Takeuchi, H. Kobayashi, *Solid State Ionics* **2016**, *285*, 112.

- [18] T. Asano, S. Yubuchi, A. Sakuda, A. Hayashi, M. Tatsumisago, *J. Electrochem. Soc.* **2017**, *164*, A3960.
- [19] A. Sakuda, A. Hayashi, Y. Takigawa, K. Higashi, M. Tatsumisago, *J. Ceram. Soc. Jpn.* **2013**, *121*, 946.
- [20] N. Kamaya, K. Homma, Y. Yamakawa, M. Hirayama, R. Kanno, M. Yonemura, T. Kamiyama, Y. Kato, S. Hama, K. Kawamoto, A. Mitsui, *Nat. Mater.* **2011**, *10*, 682.
- [21] Y. Kato, S. Hori, R. Kanno, *Adv. Energy Mater.* **2020**, *10*, 2002153.
- [22] J. Wu, L. Shen, Z. Zhang, G. Liu, Z. Wang, D. Zhou, H. Wan, X. Xu, X. Yao, *Electrochem. Energy Rev.* **2021**, *4*, 101.
- [23] Y. Jin, Q. He, G. Liu, Z. Gu, M. Wu, T. Sun, Z. Zhang, L. Huang, X. Yao, *Adv. Mater.* **2023**, *35*, 2211047.
- [24] X. Zhao, P. Xiang, J. Wu, Z. Liu, L. Shen, G. Liu, Z. Tian, L. Chen, X. Yao, *Nano Lett.* **2023**, *23*, 227.
- [25] W. J. Li, M. Hirayama, K. Suzuki, R. Kanno, *Solid State Ionics* **2016**, *285*, 136.
- [26] N. Ohta, K. Takada, I. Sakaguchi, L. Zhang, R. Ma, K. Fukuda, M. Osada, T. Sasaki, *Electrochem. Commun.* **2007**, *9*, 1486.
- [27] G. G. Amatucci, J. M. Tarascon, L. C. Klein, *J. Electrochem. Soc.* **1996**, *143*, 1114.
- [28] R. A. Huggins, *Ionics* **2002**, *8*, 300.

---

Manuscript received: June 20, 2023  
Revised manuscript received: July 19, 2023  
Accepted manuscript online: July 20, 2023  
Version of record online: August 4, 2023

---